Optimizing the HUSIR Antenna Surface

Joseph M. Usoff, Michael T. Clarke, Chao Liu, and Mark J. Silver

The primary objective of the HUSIR upgrade was to significantly improve the imaging resolution achievable by the Haystack radar. To meet this image resolution objective, a W-band (96 GHz center frequency, 3 mm wavelength) capability was added to the radar. W band provides the necessary bandwidth for high-resolution imaging, but its much smaller (than the original K band) operating wavelength makes the requirements on the antenna much more stringent and challenging to achieve.

» For a given target at a given range, the sensitivity of a radar is proportional to the transmit power and the gains of the transmitting and receiving antennas, which are the same for a monostatic radar such as the Haystack Ultrawideband Satellite Imaging Radar (HUSIR). As the operating frequency increases, it becomes more difficult to generate high transmit power, so it becomes vitally important that the gain of the antenna is maximized. The gain of a reflector antenna is inversely proportional to its surface errors in an exponential manner. Highly efficient reflector antennas require surface tolerances on the order of one-thirtieth of a wavelength or less. At HUSIR's operating wavelength of 3 mm (100 GHz), for example, the surface tolerance must be on the order of 100 μm root mean square (rms). Achieving and maintaining such a tolerance on the 120-foot-diameter HUSIR antenna is very challenging; careful design of the antenna structure, meticulous implementation of the design, and an accurate metrology system to measure the surface are required.

The efficiency of a reflector antenna is inversely proportional to the rms surface errors as shown by Ruze [1]. A simplified version of the Ruze equation that is appropriate for HUSIR is plotted in Figure 1. The original 120-foot-diameter Haystack antenna was completed in 1964, representing what was then considered the state of the art in the construction of large moving structures, with a specified surface (half-path-length error) tolerance of 0.025 inch (0.64 mm) rms [2, 3]. Several improvements were made over the years, reducing the tolerance to 0.017 inch (0.43 mm) rms in 1967 [4]. With the addition of thermal control of the back-
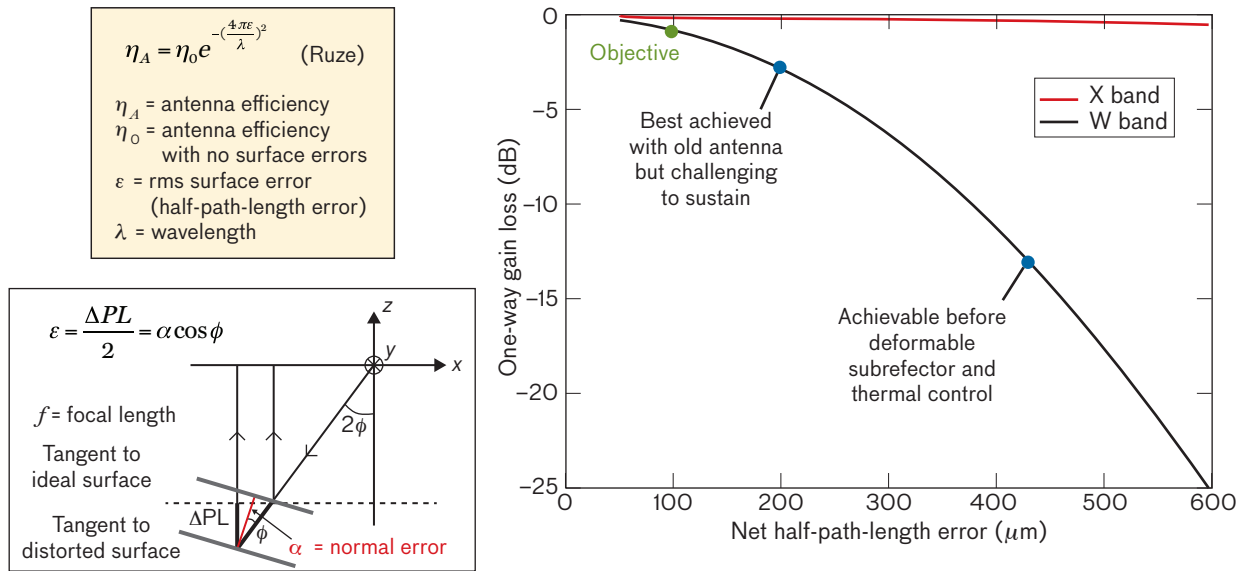
FIGURE 1. The Ruze equation relates the efficiency of a reflector antenna to its rms half-path-length error (HPLE). HPLE is a measure of the variation of a surface from the ideal that causes the phase to vary across the aperture, leading to decreased efficiency. HPLE is similar to surface normal error, but to determine path-length change, the cosine of the incident angle must be included. A change in frequency can have a large impact on antenna efficiency. The Ruze curve is shown plotted at the center frequencies of the two HUSIR operating bands, 10 GHz (red curve) and 96 GHz (black curve). At 10 GHz, there is very little variation in gain over the 600 μm HPLE range of the graph, but at 96 GHz, there is more than 20 dB of variation.

structure, improvements in the radome heating control, and a deformable subreflector, the tolerance was reduced to 0.008 inch (0.20 mm) rms in 1992 [5, 6]. It was not possible, however, to maintain the surface tolerance at the 0.20 mm level under radar operating conditions. Radar operations at Haystack are conducted throughout the year. The radome is heated in cooler months to 50°F, but the radome does not have any cooling capability, so thermal conditions, which vary significantly on warm days, distort the surface. The requirements for tracking a low-Earth-orbit (LEO) satellite are also more demanding than those for tracking a celestial source. For LEO satellites, the elevation angle of the antenna may vary from horizon pointing to zenith pointing in a matter of a few minutes, so the response time for corrective actions needs to be on the order of seconds. Analysis of the existing antenna structure indicated that the performance of the Haystack antenna had reached the limits of its capabilities and a major rebuild was required to meet W-band operational requirements.

A major goal of the antenna design for the HUSIR upgrade was to achieve a half-path-length error (HPLE)

of 100 μm rms or less under all environmental conditions over a range of elevations from 10 to 40 degrees, which roughly corresponds to the range of viewing angles sufficient to cover the geostationary belt from the antenna location in Westford, Massachusetts. Applying the Ruze equation, at a frequency of 96 GHz, 100 μm rms HPLE corresponds to an efficiency of 85%, or a one-way gain loss of –0.7 dB.

The HUSIR antenna, shown in Figure 2, is described in more detail in companion articles in this *Lincoln Laboratory Journal*. The antenna components that most directly influence the surface tolerance include the surface panels and subframes, the subreflector, and the backstructure.

Error Budget Factors

The overall surface tolerance that is achieved for an antenna is a function of gravitational distortions, thermal distortions, manufacturing tolerances of the components, and assembly tolerances. The HPLE budget for the HUSIR antenna at an elevation angle of 30° is shown in Figure 3. For additional details on these errors, see Doyle et al. [7].
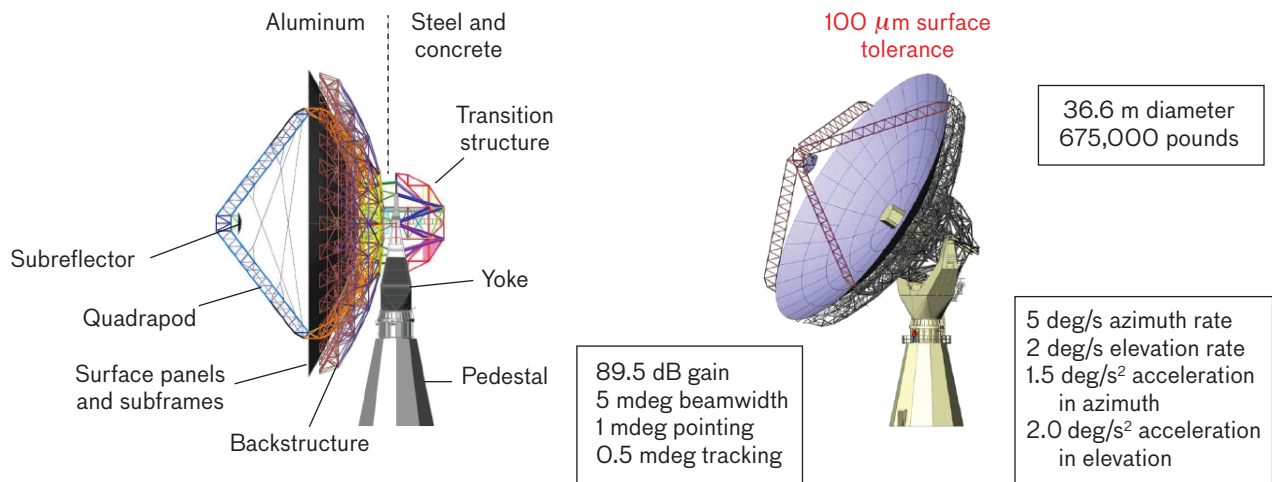
JOSEPH M. USOFF, MICHAEL T. CLARKE, CHAO LIU, AND MARK J. SILVER

FIGURE 2. The HUSIR upgrade included an almost complete replacement of the Haystack antenna. Only the pedestal and yoke were retained from the original antenna, and significant modifications to the yoke had to be made to accommodate the new antenna drives. The Cassegrain-design antenna includes a transmitted electromagnetic wave (emitted from the center of the primary reflector) that is reflected by the subreflector onto the primary reflector surface and radiated into space. Any subreflector and primary surface errors impact the efficiency of the antenna.

Gravity Effects

The antenna structure shown in Figure 2 is a homologous [8] design developed by Simpson Gumpertz & Heger Inc. (SGH) [9]. They used the Jet Propulsion Laboratory's ANTenna OPTimization flavor of NASTRAN finite element analysis software (JPL-ANTOPT NASTRAN, NASTRAN for NASA STRucture ANalysis) to optimize component sizes so that surface tolerance and weight were minimized while safety margins were maintained. In a homologous design, the parabolic shape of the surface will deform as a function of elevation angle, but the deformed surface will still be parabolic, albeit with a different focal point. The subreflector is mounted on an actuated hexapod that adjusts the subreflector position as a function of elevation to compensate for the changing focal point. However, the structure is not perfectly homologous and there are residual errors caused by gravity as shown in Figure 4. The face-up (antenna pointed at zenith) and face-side (antenna pointed at horizon) errors were computed using a detailed finite element model of the structure.

The antenna surface is divided into 432 panels mounted on 104 subframes (Figure 5). The panels were attached to the subframes while the subframes were lying flat on the floor of a thermal chamber and were not bias rigged to compensate for gravity at the rigging angle.

Therefore, gravity-induced errors of the panel-subframe units that vary with elevation must be accounted for. Bias rigging was initially considered to compensate for some of these errors, but preliminary efforts demonstrated that it would take considerable effort and expense to bias each of the subframes (a different bias is required for each subframe) for a gain of a few micrometers in the overall surface tolerance at the rigging angle. Since the subframes are attached to a curved backstructure, each subframe will have a different orientation relative to the gravity vector. A finite element model was made of each subframe, and the net gravity-induced error for all of the subframes was estimated to be 28 μm at an elevation of 30°. Similarly, the subreflector will have a gravity-induced error contribution that is not compensated for and must be included in the overall error budget. A finite element model of the subreflector estimates the gravity-induced error to be 19 μm at an elevation of 30°.

Thermal Effects

Two major contributors to the surface tolerance budget are due to temperature variations across the structure: thermal gradients and thermal lag. The antenna is enclosed in a radome that protects the antenna from the wind and weather, but the interior has only modest environmental control. The radome is heated in the winter
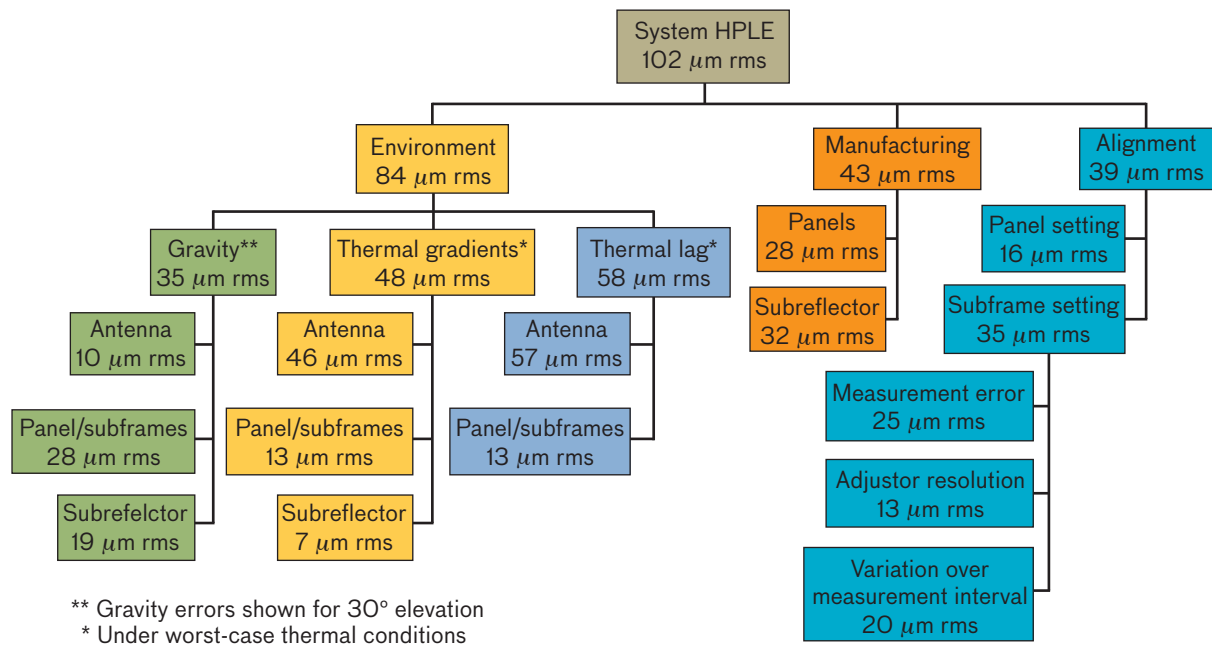
System HPLE
102 μm rms

Environment
84 μm rms

Manufacturing
43 μm rms

Alignment
39 μm rms

Gravity**
35 μm rms

Thermal gradients*
48 μm rms

Thermal lag*
58 μm rms

Panels
28 μm rms

Panel setting
16 μm rms

Antenna
10 μm rms

Antenna
46 μm rms

Antenna
57 μm rms

Subreflector
32 μm rms

Subframe setting
35 μm rms

Panel/subframes
28 μm rms

Panel/subframes
13 μm rms

Panel/subframes
13 μm rms

Measurement error
25 μm rms

Subrefelctor
19 μm rms

Subreflector
7 μm rms

Adjustor resolution
13 μm rms

Variation over
measurement interval
20 μm rms

** Gravity errors shown for 30° elevation
* Under worst-case thermal conditions

FIGURE 3. The overall error budget for the antenna surface may be subdivided into errors caused by the environment the antenna is exposed to, manufacturing errors, and alignment errors. The antenna is covered by a radome, so the environmental effects are limited to gravity and thermal effects. Gravity distortions are due to the antenna rotating in elevation such that the gravity vector orientation is changing relative to the structure. Thermal effects may be subdivided into thermal gradients, which are caused by spatial temperature variation, primarily along the ground to radome apex direction, and thermal lag, which is caused by temporal temperature variation, making antenna components with greater thermal mass expand or contract more slowly than components with lesser thermal mass. The primary surface panels and the subreflector surfaces are not adjustable, so the errors are set during the manufacturing process. The panels are first attached to the subframes and aligned relative to a theoretical paraboloid. This panel setting is accomplished in a thermally controlled chamber, utilizing a laser radar to measure the surface. The subframes are attached to the backstructure and iteratively aligned to a best-fit paraboloid of the entire surface. This process is called subframe setting.

but not cooled in the warmer months. In addition, the limited air circulation is provided by fans at a low height and a passive vent at the apex. Finally, the radome skin material is not entirely opaque to sunlight, so there is also nonuniform solar heating of the structure.

Temperature probes have been placed at multiple locations on the antenna and along the inside of the radome from the floor to the apex, and their data have been recorded and analyzed [10]. The data indicate that the antenna experiences vertical temperature gradients of up to 5°C and that the diurnal temperature variation of the air inside the radome can reach 17°C. Finite element modeling of the antenna indicates that, in the worst case, thermal gradients lead to a 46 μm rms HPLE for the main antenna structure, 13 μm for the subframes, and 7 μm for the subreflector.

The antenna is constructed of a wide variety of structural members of varying thicknesses, which therefore also have varying thermal time constants. Diurnal temperature variations lead to thermal-lag errors that can greatly exceed the overall error budget if left uncorrected. Doyle showed that most of the thermal-lag errors could be removed by adjusting the position of the subreflector, yielding a worst-case residual error of 58 μm [11]. This adjustment is currently completed several times a day by tracking a large satellite in geosynchronous orbit and adjusting the position of the subreflector to maximize the signal. Efforts are under way to fully automate the subreflector positioning in response to temperature measurements of structural elements.

Component Manufacturing

The components that make up the reflective surface include the panels and the subreflector. No alignment may remove any intrinsic manufacturing errors of the surface components from the total surface tolerance.

$$HPLE_{\mathrm{rms}}(\theta) = \sqrt{FU^2(\sin\theta - \sin\theta_o)^2 + FS^2(\cos\theta - \cos\theta_o)^2}$$
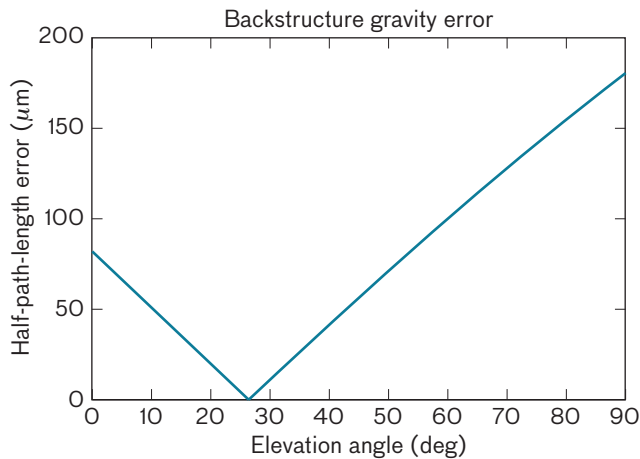
where
θ = elevation angle
θ_o = bias rigging angle = 26.7°
FU = face-up rms gravity sag = 176 μm
FS = face-side rms gravity sag = 171 μm

FIGURE 4. The backstructure will deform as the structure is rotated in elevation. Most of the deformation may be compensated for by repositioning the subreflector, but there is a small residual error that cannot be removed. The error is minimized at the rigging angle, which is the elevation angle at which the surface errors are measured and the subframes are adjusted. The half-path-length error (HPLE) was calculated using the equation above. The HUSIR rigging angle was chosen to be in the middle of the 10–40° elevation range commonly used for radar observations of the geostationary satellite belt.

Panels

The antenna surface is divided into five rings, each ring is divided into 8, 16, or 32 radial subframes, and each subframe is divided into panels as shown in Figure 5. The 432 total panels are divided into five types matching each ring, (from center to outer ring) 32 of type A, 64 of B, 80 of C, 128 of D, and 128 of E.

The panels of each type are fabricated in the same manner and are interchangeable. They are fabricated by laying a precut sheet of tension-leveled 0.063-inch-thick aluminum onto a male mold with vacuum grooves that are used to hold the sheet tight to the mold. Ribs are attached to the back of the sheet by using epoxy and straps, and doubler plates are then attached to the back of the ribs with epoxy and rivets. All parts are aligned and held in position during curing by using an assembly jig as shown in Figure 6. Upon completion, each panel was measured and the aggregate area-weighted surface accuracy of the 432 panels was found to be 28 μm rms.

Subreflector

The subreflector is a machined aluminum casting of a 112-inch (2.8 m)-diameter hyperboloid (Figure 7) with a surface accuracy of 32 μm rms. The subreflector is supported by an actuated hexapod that enables motion of the subreflector in x, y, z, and two rotation axes.
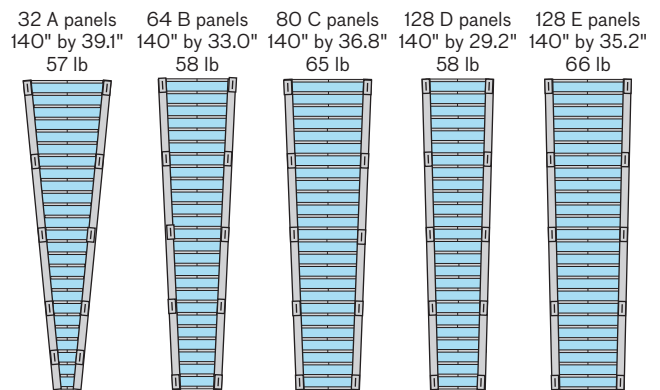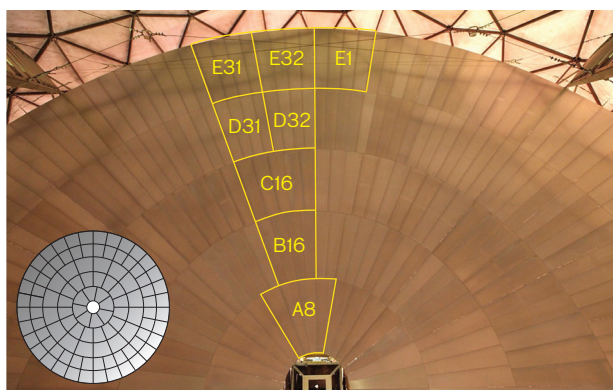

FIGURE 5. The primary antenna surface is formed of panels that are approximately 3 feet wide and 12 feet long arranged in five concentric rings.
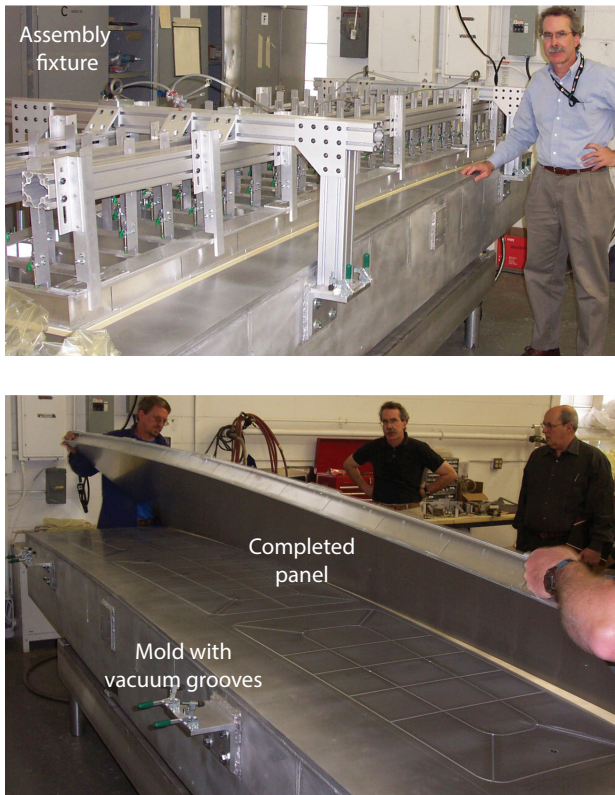
FIGURE 6. The shape of a panel is set by placing a sheet of aluminum onto a mold and applying a vacuum to ensure intimate contact. A grid of ribs is epoxied to the back of the sheet and the assembly is left to cure for 24 hours. After curing, the assembly fixture is removed, the vacuum pump is turned off, and the completed panel is removed.

Alignment

Panel-to-Subframe Alignment

Each panel is bolted at 10 attachment points along the panel periphery to a stiff truss structure called a subframe—panel types A, B, D, and E each have four panels per subframe, and panel type C has five. The panels are attached and aligned in a thermally stabilized room, utilizing a coherent laser radar (CLR) to measure the surface (Figure 8). The surface is measured and compared to a theoretical paraboloid. The attachment bolts are adjusted and the process iterated until the alignment tolerance has converged to an acceptable level. This level varies with subframe ring. The surface measurements are recorded for later use in aligning each subframe to the backstructure. The area-weighted HPLE achieved was 33 μm rms, implying that the panel-to-subframe alignment errors are 16 μm rms in combination with the 28 μm rms

panels. This process is completed once for each subframe, and the connections are locked and not adjusted again. All subsequent adjustments of the surface are completed using the subframe-to-backstructure connection.

Subframe-to-Backstructure Alignment

Each subframe is bolted to the backstructure at four points. The attachment mechanism allows for limited side-to-side motion to set the gaps between subframes, and each of the four points has both coarse and fine height adjustment capability as shown in Figure 9. Coarse height adjustments cover a range of ±16 mm with a minimum step size of 176 μm, and fine height adjustments cover a range of ±762 μm with a step size of 25 μm. The fine adjustment of the subframes is the final step in aligning the antenna surface.

Surface Measurement Techniques

Measurement of the surface to determine the required adjustments is challenging because of the limited access to the surface inside the radome, the large size of the surface, and variation of the surface over time caused by thermal effects. Four different measurement techniques were evaluated as shown in Table 1. Theodolites cannot provide the required accuracy, and the measurement process is slow. The radome makes it infeasible to use photogrammetry. Ruling out these methods leaves two possible options: CLR surface mapping and microwave holography. Unlike laser trackers that utilize a retroreflector slid along the surface, CLRs are able to directly measure reflections from the surface without physical contact. This ability is a large advantage in situations like that of the HUSIR antenna in which access to the surface is limited (no walking on the panels is permitted). A CLR was used very effectively to align the panels to the subframes, so it was natural to attempt to use a CLR to align the subframes to the backstructure. However, the CLR did not provide sufficient accuracy in the radome environment to meet the HUSIR surface alignment requirements. Microwave holography ended up being the measurement technique of choice.

The subframes were coarsely aligned using laser trackers during the subframe installation process to set the gaps between the subframes (nominally 3 mm) and to get the surface tolerance within ~1 mm rms. Once all of the subframes were installed, a CLR was used to align the surface to the desired paraboloid.
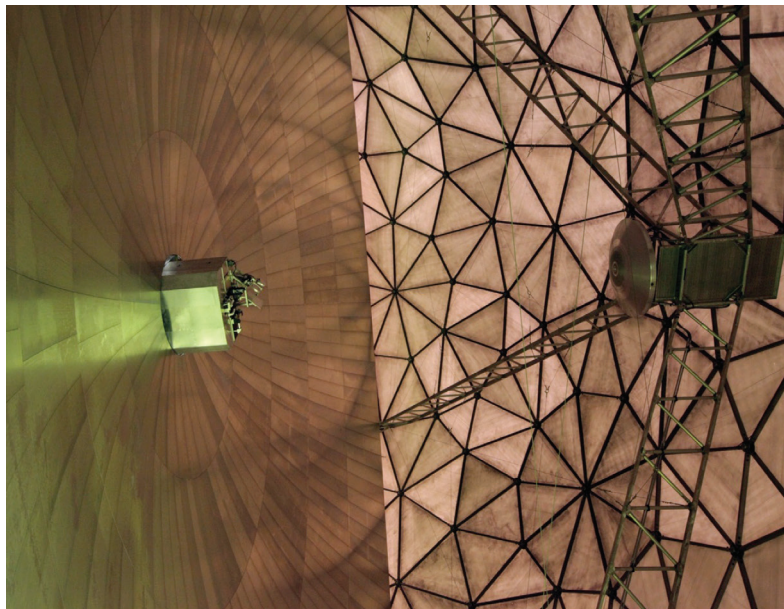
FIGURE 7. The subreflector is a 112-inch (2.8 m)-diameter hyperboloid. It was fabricated from an aluminum casting that was subsequently machined to a 32 μm rms surface accuracy. The subreflector is mounted near the apex of the quadrapod on six actuators that permit displacement and rotation of the subreflector along three orthogonal axes.
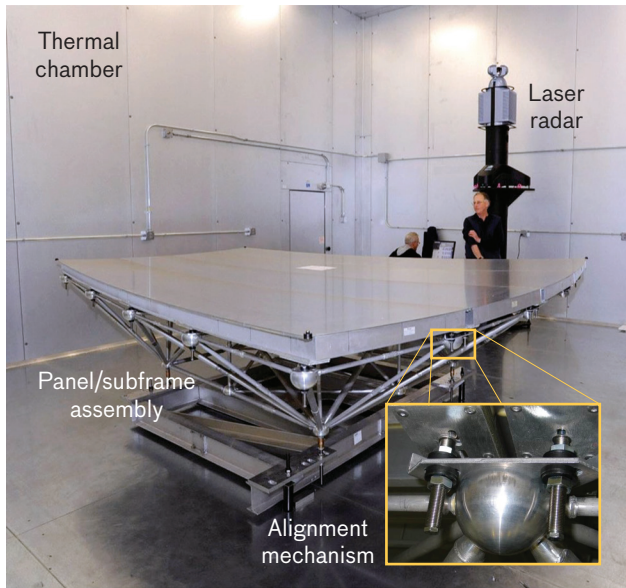
FIGURE 8. The primary surface panels are aligned to the subframes in a thermally controlled chamber by using a coherent laser radar to quickly and accurately determine the alignment of the panels to a theoretical paraboloid.

Coherent Laser Radar Alignment

A Metris MV260 CLR was mounted to the quadrapod apex (prior to subreflector attachment) as shown in Figure 10. The CLR scanned four points on each subframe, one over each adjuster, to determine the location and orientation of the subframe. The surface height errors for each of those four points, relative to a perfect paraboloid, had been previously measured and stored during the panel alignment process. All 416 points were measured, a paraboloid was fitted to the data, and off-

sets for each subframe point were calculated based on the saved measurements. Adjustments were made to the subframes and the process was repeated until convergence was reached.

Because of the positioning of the CLR and the geometry of the antenna, the CLR was not able to scan the entire surface without being reoriented. One scan was made with the CLR tilted down and one with the CLR tilted up as shown in Figure 11. Overlapping targets were used to verify the alignment of the two datasets.

CLR Alignment Results

It was discovered that the data for the overlapping targets did not agree between the CLR tilted up and CLR tilted down measurements. It was determined that the CLR was not able to maintain calibration when tilted down. The CLR was removed from the antenna, and an attempt was made to calibrate the CLR in both the tilt-up and tilt-down orientations. A separate calibration file was maintained for each orientation. The CLR was then remounted onto the antenna, and alignment of the surface proceeded.

An iterative measure-and-adjust process was followed until convergence was reached. It was found that the measurement accuracy of the CLR in the tilt-down orientation was not sufficient to complete the surface alignment to the required tolerance. Subsequent high-resolution scans of some of the upper subframes indicated that their alignment errors exceeded the budget, suggesting that alignment based on measurements at only the four fiduciary points per subframe was not sufficient.

After the initial alignment process was terminated and testing of the antenna control system was under way,

Table 1. Comparison of Antenna Surface Measurement Techniques

| TECHNIQUE	ACCURACY	TIMELINESS	PRACTICALITY	COMMENTS
Theodolite	Poor	Poor	Good	Typically 500 mm accuracy Slow process for any points on a large disk
Photogrammetry	Good	Good	Poor	Cannot acquire measurements with radome in place
Coherent laser radar	Good	Moderate	Moderate	Instrument loses calibration when tilted Slow for dense sampling
Microwave holography	Good	Good	Good	Established radio-astronomy technique Requires compensation for radome and subreflection diffraction
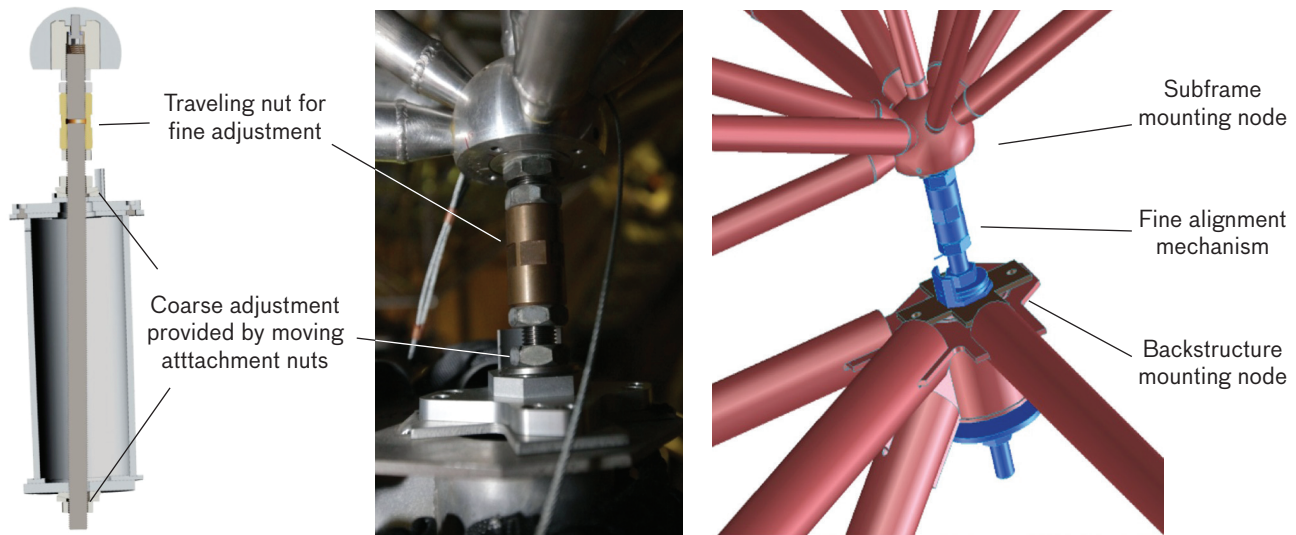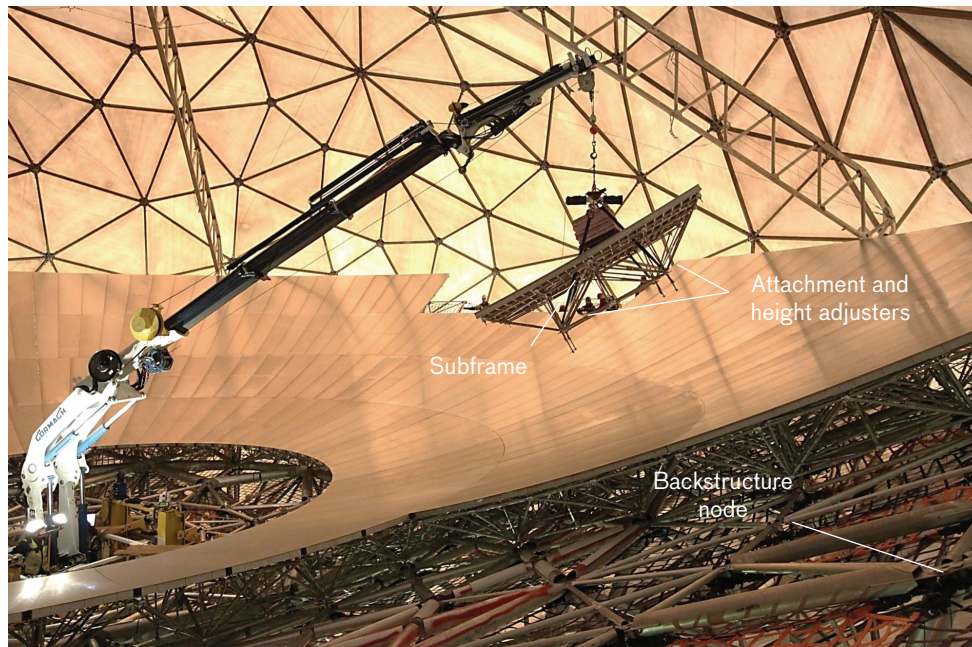
FIGURE 9. Subframes are attached to the backstructure with a bolted connection that includes coarse and fine height adjustment capabilities. Subframes are initially aligned during the installation process by using laser trackers located near the vertex of the primary reflector. This initial alignment resulted in an accuracy of ~1 mm in height and equalized the gaps between the subframes.

some of the subframes had moved and were in contact with their neighbors. Further investigation revealed that thermal flexures located between the subframe adjusters and the subframe nodes were failing. The subframe-to-backstructure connection was redesigned without a flexure, and all subframe connections were replaced with the new design. A process was developed to limit the subframe movement during replacement, but the surface

alignment attained with the CLR was compromised and a new alignment was required. The insufficient results of the initial CLR alignment approach led to abandoning CLR in favor of microwave holography for subsequent surface alignment. However, the initial alignment effort with the CLR did achieve a surface with a focused beam and good antenna efficiency at 20 GHz (K band), which was required for microwave holography.
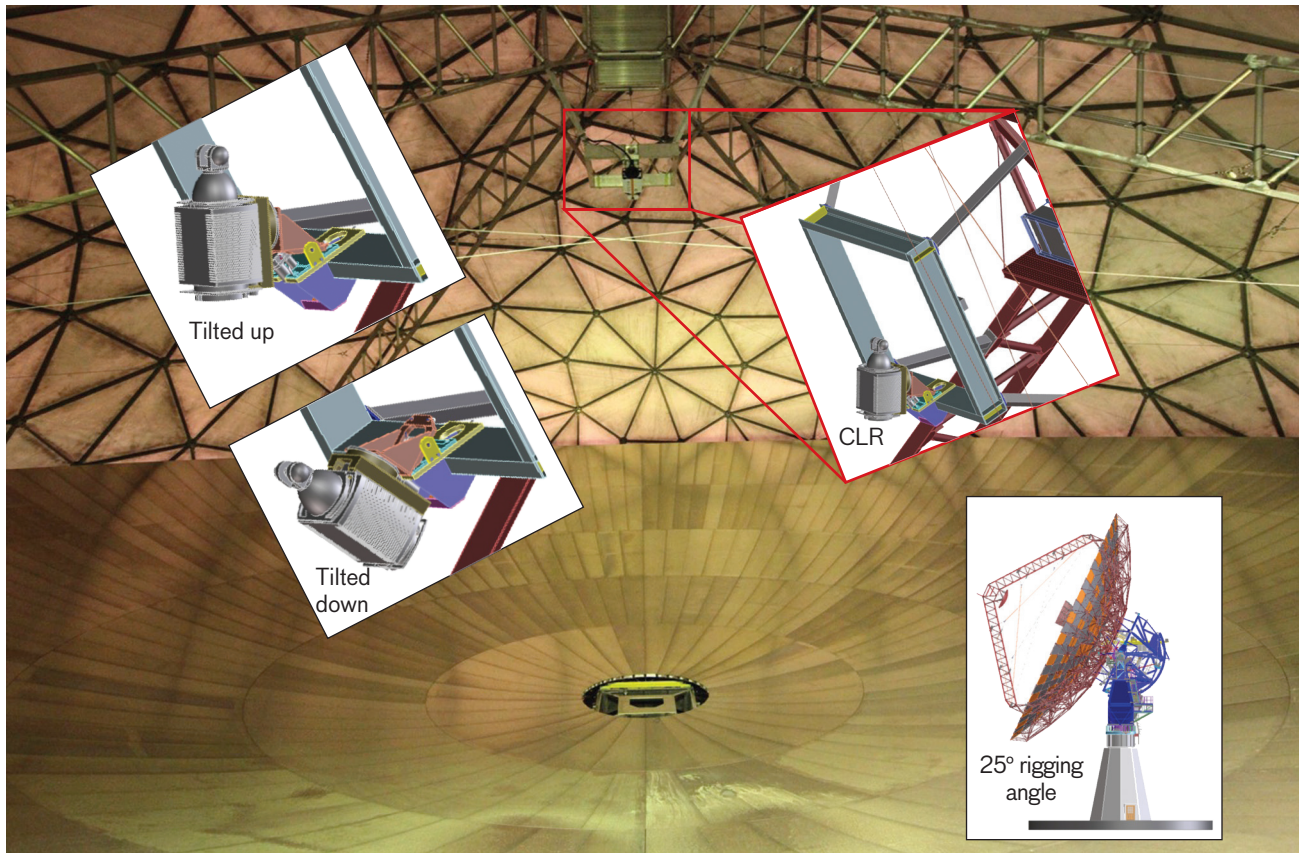
FIGURE 10. A coherent laser radar (CLR) was mounted near the apex of the quadrapod so that the surface could be scanned. The entire surface could not be scanned with the CLR in a single orientation because of its proximity to the surface and its limited range of motion. As a result, the upper portion of the surface was scanned with the CLR at one orientation and then the CLR was tilted and the lower portion of the surface was scanned.

Microwave Holography Alignment

Microwave holography is a measurement and analysis technique that provides a detailed map of an antenna's surface. The measured map is compared to the ideal surface and the subframes are adjusted to minimize the difference. This process of measure, analyze, and adjust is iterated until the surface tolerance meets the objective or until the limits of the process are reached.

The relationship between the complex far field of an antenna and its reflector-surface errors has been recognized and exploited for antenna surface alignment since the mid-1970s [12–17]. Most large, precise, radio-astronomy antennas in the world have been aligned using holographic techniques, and JPL has used microwave holography extensively to align the surfaces of its deep-space network of antennas [18–20].

The main concept underlying microwave holography is that there is a known relationship between the field over an aperture and the field at a remote point P. Following Silver [21], let the aperture lie in the x-y plane, as shown in Figure 12 with coordinates of a point in the aperture at $(\xi, \eta, 0)$, the remote field point P at (x, y, z), and the field over the aperture designated as $f(\xi, \eta)$. The field $f(x, y, z)$ at P is given by

$$f(x,y,z) = \int F(\xi,\eta) \frac{e^{-jkr}}{4\pi r}\left[\left(jk + \frac{1}{r}\right)\mathbf{i}_z \cdot \mathbf{r}_1 + jk\mathbf{i}_z \cdot \mathbf{s}\right]d\xi d\eta,$$

where $k = 2\pi/\lambda$ is the wavenumber, s is the unit vector in the direction of a ray at a given point in the aperture, $\mathbf{r}_1$ is a unit vector from the aperture point to the field point, and $\mathbf{i}_z$ is the unit vector in the $\mathbf{z}$ direction, which is normal to the aperture.

This expression may be simplified in the far field for
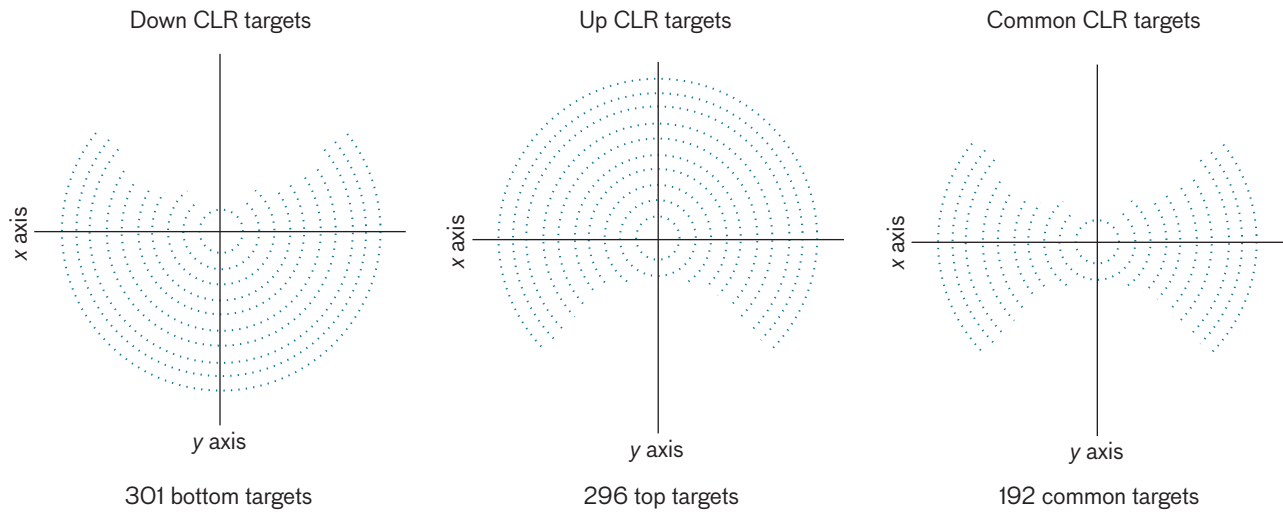
FIGURE 11. The CLR could not scan the entire surface while in a single orientation. There were four target points on each subframe, for a total of 416 points. The lower 301 target points were visible with the CLR tilted down, and the upper 296 target points were visible with the CLR tilted up. There were 192 common target points that helped to align the data and to validate the accuracy.

angles close to the normal direction and for small phase errors over the aperture to

$$f(u,v) \approx j2k\frac{e^{-jkR}}{4\pi R}\int F(\xi,\eta)e^{jk(\xi u+\eta v)}d\xi d\eta,$$

where u and v are direction cosines given as

$$u = \sin\theta\cos\phi$$

$$v = \sin\theta\sin\phi$$

with (θ, φ) being the usual spherical coordinates. This is an expression of Huygens' principle, where each point on a wavefront may be regarded as a source of a spherical wave and the value of the field at a remote point is a superposition of spherical waves. It may also be seen that there is a Fourier transform relationship between $f(u, v)$ and $F(\xi, \eta)$. The inverse relationship is given by

$$F(\xi,\eta) \propto \int f(u,v)e^{-jk(\xi u+\eta v)}dudv.$$

This inverse relationship is used to determine the fields in the aperture from the measured far-field-pattern data.

Geometric optics is used to relate the aperture field to the main reflector surface. Ray tracing from the phase center of the feed to the subreflector to the aperture plane shows that the phase will vary with path-length irregularities. For an ideal parabola and matched hyperbolic subreflector, the path length is identical for every ray and the phase is uniform across the aperture. For a nonideal surface or mismatch of surface and subreflector, path-length changes result in phase variations across the aperture. The geometric relationship between a surface distortion and the change in path length is shown in the lower left of Figure 1. The surface normal error is therefore related to the measured phase error by

$$\delta_n = \frac{\text{phasor error}}{2k\cos\phi},$$

where for a parabola of focal length F

$$\cos\phi = \frac{1}{\sqrt{1+\dfrac{x^2+y^2}{4F^2}}}F.$$

The measured pattern will be distorted by diffraction from the subreflector and its support structure. This distortion must be subtracted before surface corrections are made. In addition, scattering from the radome's spars and hubs had to considered before aligning the HUSIR antenna surface. HUSIR is unique in that it is the only antenna that has been reported to use holography for alignment while residing inside a space-frame radome [22].

Any measurement system exhibits some drift during the time that it takes to collect data. This drift may be removed by collecting calibration information through-
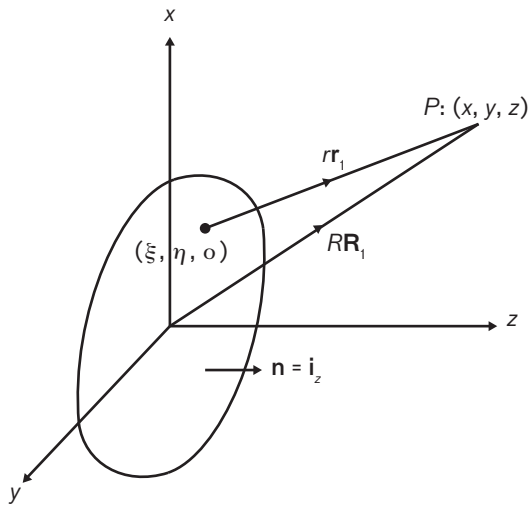
FIGURE 12. Without loss of generality, let the aperture lie in the *x-y* plane [21]. The far field at angles close to the *z* axis is a Fourier transform of the aperture field.

out the data collection period. For microwave holography systems, this continuous recalibration is commonly done by repeatedly returning to the center of the scan where there should be no variation in the signal for an ideal system.

By applying the geometric optics relationship outlined above, the phase errors are matched to surface positions and the data are fit to a paraboloid. The residuals between the data and the best-fit paraboloid represent the surface errors.

A finite element NASTRAN model was generated for each of the five subframe types and used to determine the surface distortions that arise by turning each adjuster. An example of a model and the resulting deformations is shown in Figure 13. These deformations form the basis parameters for determining the number of nut turns (or partial nut turns) to apply to each subframe attachment assembly to reduce the residual error calculated from the data.

The steps in the holographic process are

1. measure the complex far field,
2. correct for system drift during the measurement period,
3. transform the data to the aperture plane,
4. subtract diffraction caused by the radome, subreflector, and any aperture phase nonuniformities due to the feed pattern,
5. relate the aperture phase to the surface using geo-

metric optics, fit the data to a paraboloid, and find the residual errors,

6. determine the adjuster turns to minimize the errors, and
7. iterate.

Microwave Holography Subsystem

The objective of using the holography subsystem was to accurately measure the complex far-field pattern of the HUSIR antenna. The signal received from a geostationary satellite as a function of the HUSIR antenna orientation provided the necessary far-field pattern. The amplitude and phase of the signal coming from the satellite vary randomly, and those variations must be removed from the measurements to determine the variations that are due to the antenna pattern. This elimination was accomplished using a reference antenna located near the HUSIR antenna as shown in Figure 14. Any amplitude and phase variations in the signal will be common to both the HUSIR antenna and the reference antenna. The reference antenna was aligned to maximize the signal from the satellite and then fixed in that orientation. The complex pattern of the HUSIR antenna was measured by scanning the HUSIR antenna over a range of angles and recording the cross-correlation of the HUSIR and reference antenna signals normalized by the autocorrelation of the fixed reference antenna. Cross-correlation and normalization removed variations in the signal that are common to the two antennas, leaving the amplitude and phase variation that were due to the pattern of the HUSIR antenna alone.

There are no geostationary satellites that radiate at W band, but there are satellites providing Internet service that radiate in the 19.7 to 20.2 GHz band. This bandwidth is fortuitous for HUSIR as it permits use of the radio-astronomy K-band feed, which is mounted directly below the radar feeds as shown in Figure 15. A geostationary satellite at 111.1°W was chosen to be the source because its elevation relative to HUSIR is 26.7°, which is close to the center of the HUSIR's 10- to 40-degree geostationary belt observation window. The downlink has 57 dB of equivalent isotropically radiated power (EIRP) and includes eight 54 MHz channels.

The front ends of the reference antenna and HUSIR K-band receivers have low-noise amplifiers that feed radio-frequency-over-fiber links to the control room as shown in Figure 16. Each channel is then downconverted to 60 MHz by using common local oscillators to mini-
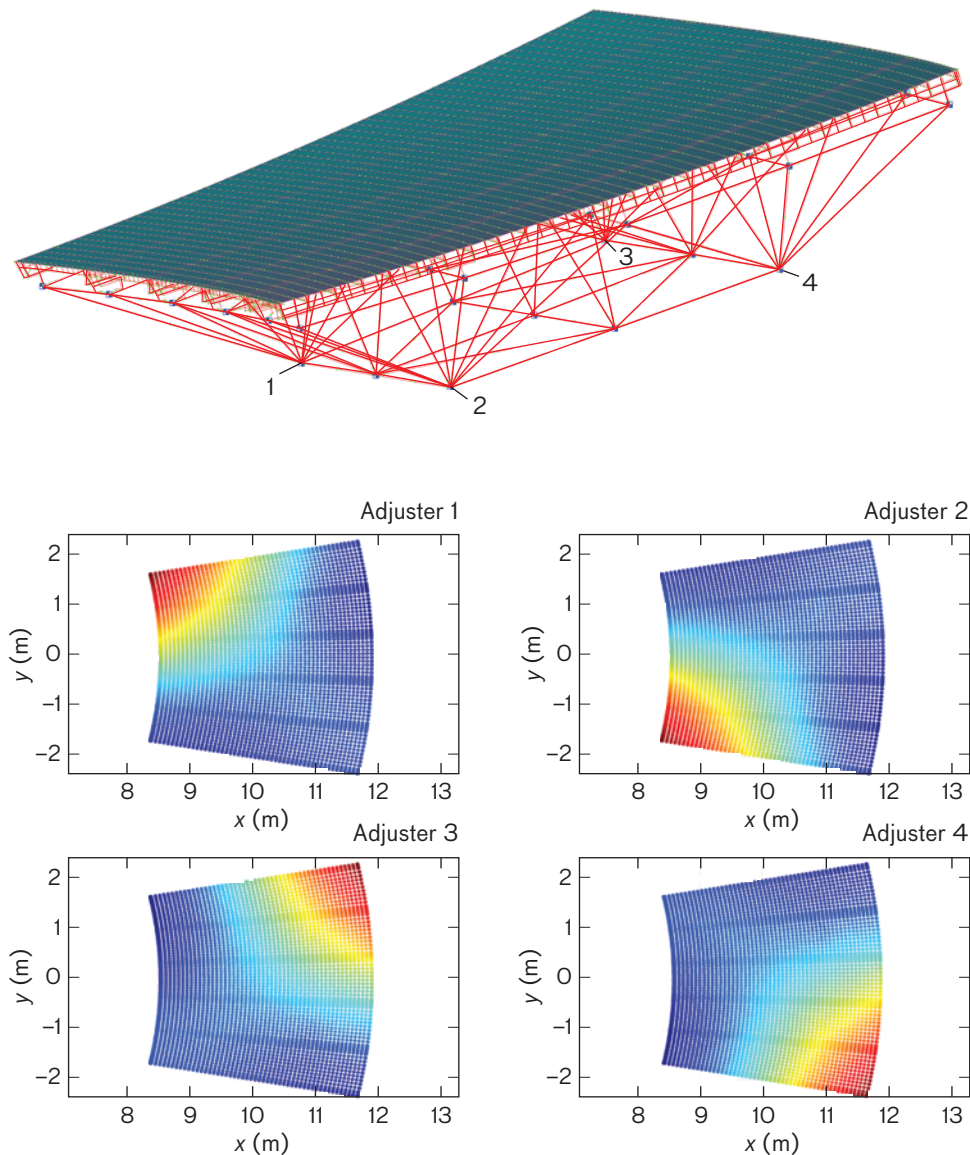
FIGURE 13. A finite element model was generated for each type of subframe. The distortion of the surface was calculated for the motion of a single attachment point while the others remain fixed.

mize phase errors between the two receivers. Bandwidth is set at 20 MHz, which provides sufficient resolution for the separation of multipath reflections from the desired direct signal. A commercial signal processing board digitizes the signal and performs signal integration and cross-correlation in real time. The peak of the cross-correlation is recorded along with an inter-range instrumentation group (IRIG) time stamp.

The reference antenna signal is peaked on the satellite signal and then fixed in that position. The HUSIR antenna is scanned in a pattern that meets Nyquist sam-

pling requirements and frequently returns to the peak position to measure phase and amplitude drift. Raster-like scans are commonly used to collect pattern data, but they require the antenna to make a sharp turn at the end of each scan line and they do not normally make frequent returns to the center position. The HUSIR holography system uses a hypotrochoid scan as shown in Figure 17. HUSIR utilizes a scan pattern with the large fixed circle radius set to be 256 times as large as the rolling small circle radius and the attachment point radius set to be 255 times the small circle radius. The scan rates were
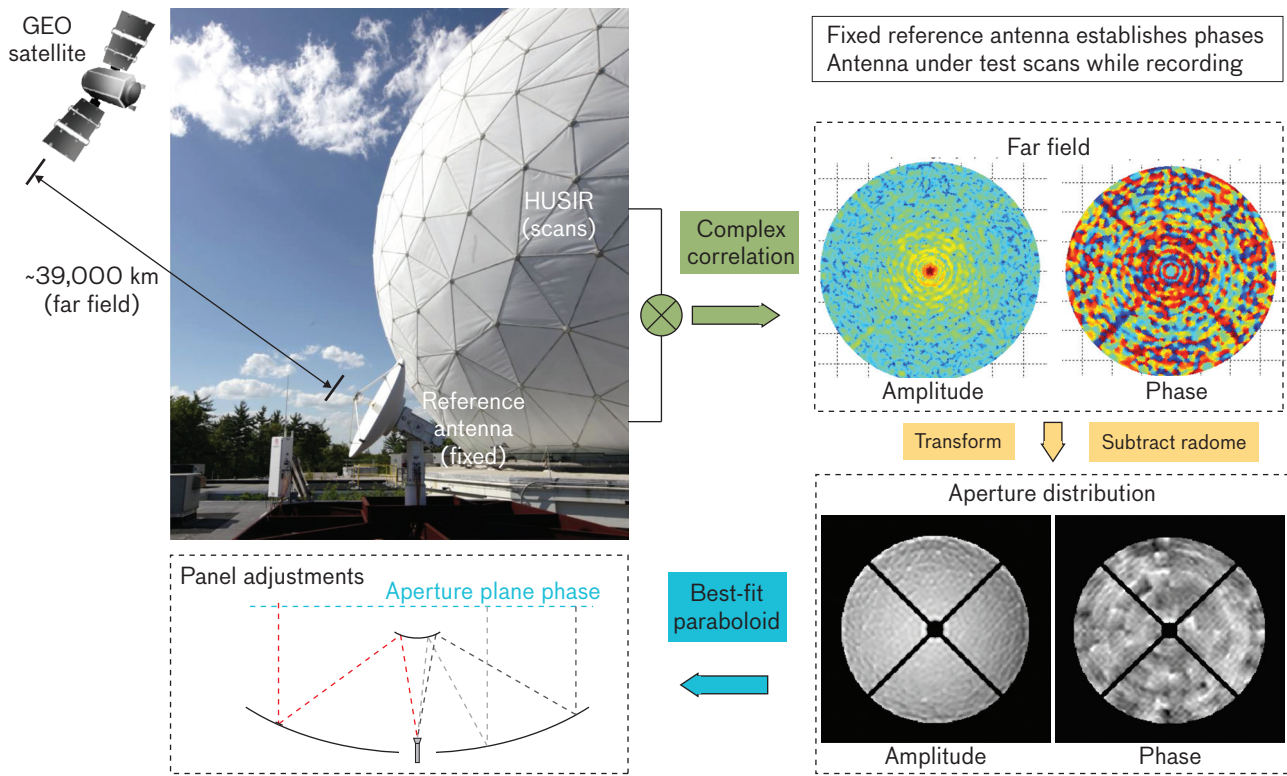
FIGURE 14. Using a geostationary (GEO) satellite as a signal source, the HUSIR holography system collects the complex far-field pattern of the HUSIR antenna. A nearby reference antenna tracks the phase of the signal. The far-field pattern is transformed to the aperture plane, and the required surface adjustments are determined by the relationship between the phase of the aperture plane and variations in the surface of the antenna.

set to match a rotation rate of 1 rad/s for the small circle, so the scan returns to the center position every 2π or ~6.3 seconds and the complete scan takes 512π seconds or ~27 minutes. Using this scan pattern was found to be much faster than using a raster scan. It is desirable to minimize the time that the scan takes so that thermal variations are minimized as well. This scan rate is also about as fast as the antenna can move and accurately follows the hypotrochoid pattern.

Typical measured phase drift over a holography scan is shown in Figure 18. Ideally this curve would be flat, but there are differences between the two signal paths that must be accounted for to generate an accurate surface map. The long slow variations are due to thermal effects, and the shorter timescale variations are due to atmospheric effects and antenna vibrations.

The angular extent (θ_{max}) of the scan and the wavelength (λ) determine the spatial resolution (δ) of the surface map:

$$\delta \cong \frac{\lambda}{2\theta_{max}} \quad .$$

There is a trade-off between spatial resolution and the accuracy of the holography map. Larger scan angles yield better resolution, but larger scan angles take longer to collect. The thermal environment in the radome is constantly varying, so longer scan times can result in more thermal variation and reduced accuracy. To help determine what scan range to use, we consulted with engineers at JPL who have extensive experience in using holography to align antenna surfaces. JPL had determined that ~25 sample points are required on each surface component that is to be aligned. HUSIR subframes vary in size from approximately 3.6 m × 3.0 m for the D ring to 3.6 m × 4.7 m for the C ring. For a holography wavelength of ~1.5 cm, a scan extent of ±0.7° provides 0.6 m spatial resolution and meets the criterion of 25 sample points per subframe criteria. This scan extent was established as the standard during the alignment process.
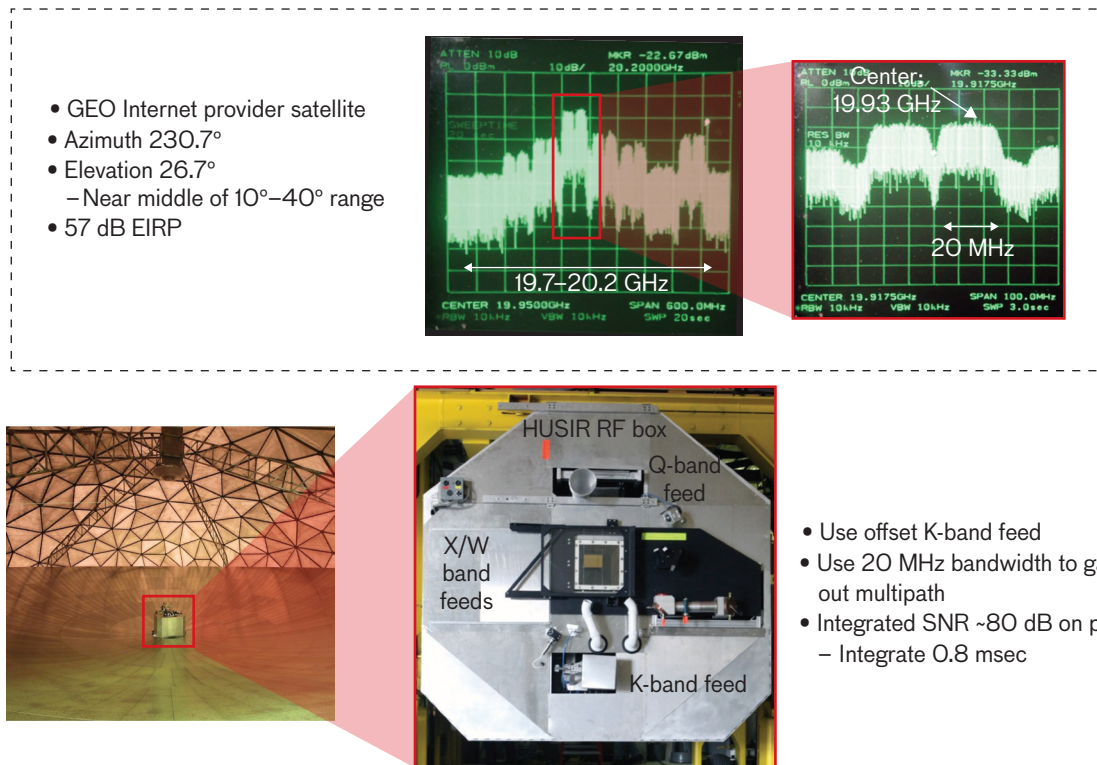
FIGURE 15. The HUSIR holography system utilizes an offset K-band feed that is otherwise used for radio-astronomy measurements. The chosen source satellite is an Internet service provider that emits a wideband signal centered near 19.93 GHz.

The accuracy (Δ) of the holography measurement is inversely proportional to the beam peak voltage signal-to-noise ratio (SNR) of the test antenna [14, 20]:

$$\Delta \cong \frac{\lambda D}{4\pi\delta \cdot SNR} = \frac{D\theta_{max}}{2\pi \cdot SNR},$$

where D is the test antenna diameter. For the HUSIR antenna and a ±0.7° scan, a 20 μm accuracy requires a 71 dB power SNR as seen in Figure 19.

The link budget between the geostationary satellite and the HUSIR antenna indicates that the power SNR is ~40 dB, which may be increased by integrating the signal over time. The signal is sampled at an 80 MHz rate and 65,536 samples or ~0.8 msec of data are integrated. With integration gain, the power SNR is in excess of 80 dB, leaving significant margin to allow for atmospheric attenuation, beam pointing losses, and degradation of transmitted power from the satellite amplifiers.

This estimate of the accuracy does not account for the thermal variation that occurs during the data collection period. Thermal variation is more difficult to assess since it is a function of the unknown thermal conditions during the data collection. Measurement accuracy may be assessed by repeating the measurements without making any changes and examining the difference between results.

Post-processing was completed on a laptop computer by using MATLAB and followed the flow shown in Figure 20. Total processing time was typically five minutes or less. The two steps requiring the most processing time were the transformation of the far field to the aperture field, since this was completed with a Fourier sum, and the calculation of the radome diffraction. Small changes in the satellite position required recalculating the radome diffraction for every dataset.

Microwave Holography Results

To minimize interference, holography data collection occurs at night after all other radars are off the air and at least five hours after sunset to minimize thermal variation during the measurement interval. Initially, a narrow sparse scan run to precisely locate the satellite typically takes less than five minutes to complete and ensures that the return to center
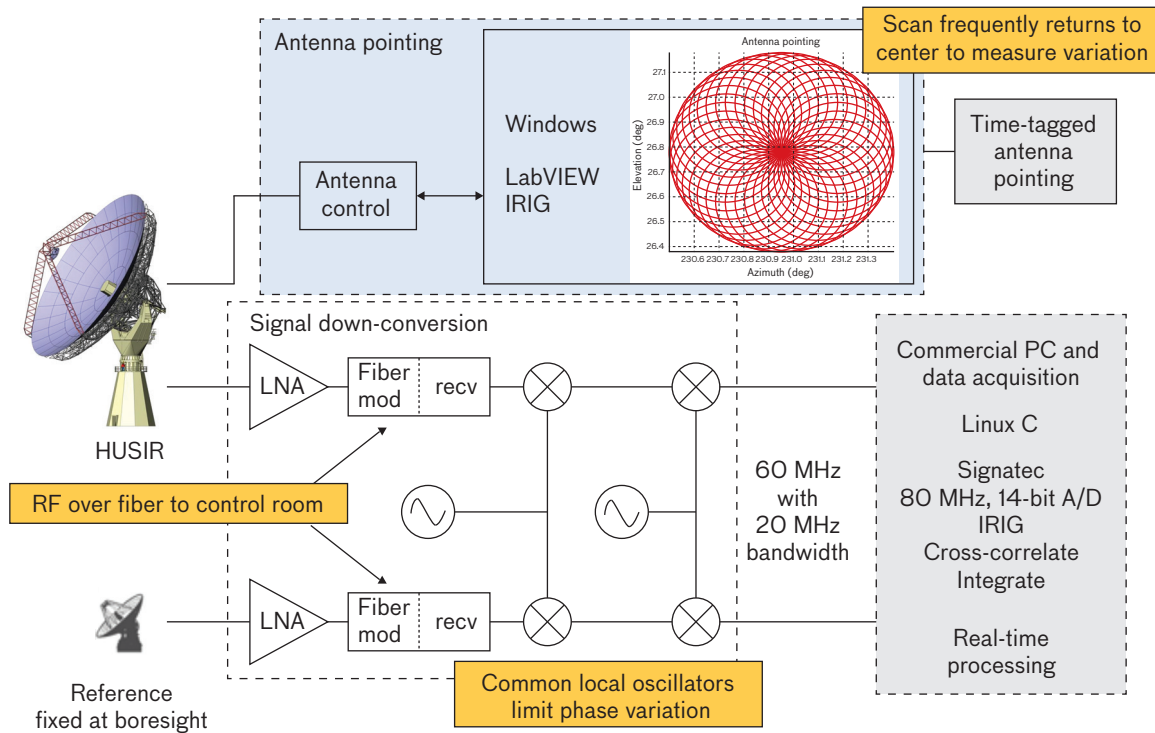
FIGURE 16. The holography system measures and correlates the signals from the HUSIR antenna and the reference antenna. The receivers share common local oscillators to minimize phase drifts between the two. The reference antenna stares at the satellite while the HUSIR antenna is scanned in a hypotrochoid pattern. A commercial PC and signal processing board perform real-time correlation and data recording. LNA stands for low-noise amplifier.
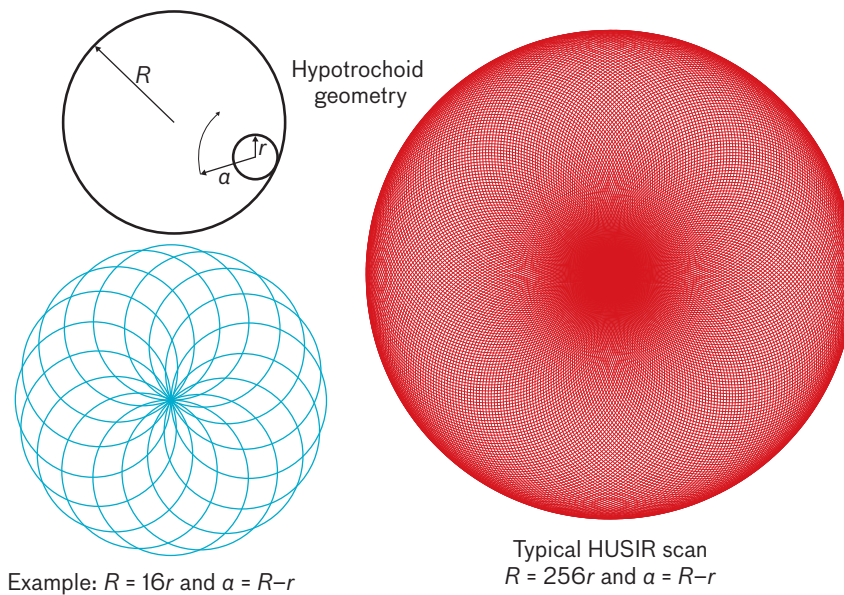

Example: $R = 16r$ and $\alpha = R-r$

Typical HUSIR scan
$R = 256r$ and $\alpha = R-r$

FIGURE 17. The HUSIR far-field pattern is collected by scannning the antenna along a hypotrochoid path. A hypotrochoid is generated by tracing a point that is attached to a smaller circle as it rotates along the inside of a larger circle. If the radius of the attachment point is chosen to be the difference between the circle radii, the trace will return to the center of the large circle every time the smaller circle makes a complete revolution. The curve that was traced to collect the HUSIR pattern data is shown in red.
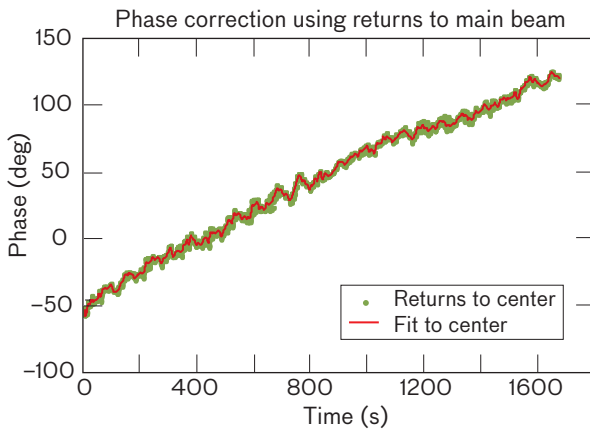
FIGURE 18. When the HUSIR antenna is boresighted on the satellite, the phase of the correlation between the two antennas should not vary. This plot shows the phase of the correlation as a function of time with the green dots marking where the HUSIR antenna has returned to the boresight orientation. If the system were perfect, the green dots would lie on a straight horizontal line, but they clearly do not. There is a large slope to the data that comes from thermal variation over time of one fiber path compared to the other. Small perturbations seen on a shorter timescale are likely due to atmospheric path differences and/or vibrations of one antenna relative to the other. This return-to-center phase variation is used to correct the recorded correlation data before they are transformed to the aperture plane.

FIGURE 19. Surface tolerance measurement accuracy is a function of the peak signal-to-noise ratio (SNR), the diameter of the antenna being tested, and the extent of the scan. To achieve a 20 μm measurement accuracy for the HUSIR holography measurements, the peak power SNR is required to be 71 dB or greater.

phase corrections will be accurate. As soon as a scan is completed, the location of the far-field-pattern peak is found and the next scan is begun centered on the peak location. The antenna pointing and far-field data files are transferred to a laptop and post-processing is completed while the next scan is collected. At least two full scans are made during each data collection, and the difference between the collections is used to indicate system stability and data quality.

A typical far-field pattern is shown in Figure 21. Rings of sidelobes are clearly evident as are peaks along the 45° axes that are due to scattering from the quadrapod legs.

The far-field pattern is interpolated to a uniform grid and transformed to the aperture plane using a discrete Fourier transform, and corrections are made for radome and subreflector scattering, as shown in Figure 22. Outlines of individual subframes apparent in the aperture-phase data indicate that the subframes are not properly aligned. If all of the subframes were aligned to a paraboloid, the phase would be uniform across the aperture and the aperture field phase would be displayed as solid gray. Phase varia-
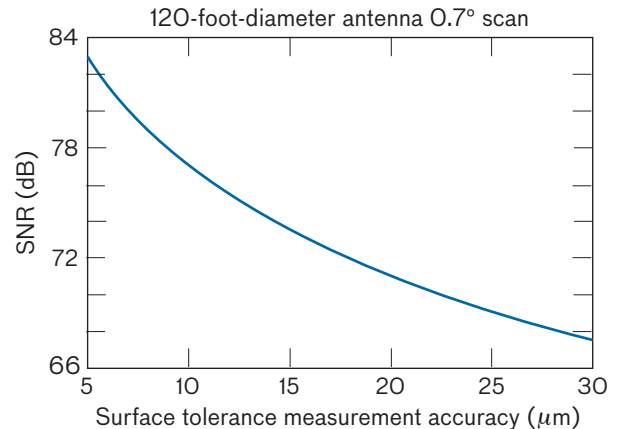
tion from the feed was measured in a compact range and the contribution was found to be negligible, so feed corrections were not necessary. The areas that were shadowed by the quadrapod and the subreflector were masked and were not used to calculate the surface adjustments.

The aperture phase is converted to path length and a paraboloid is fit in a least-squares sense to the data. In general, seven parameters are used in the fit: translations (dx, dy, dz), rotations (Θ_x, Θ_y), focal length change (dF), and a constant. It is possible to reposition the subreflector to remove these offsets, but care must be taken not to rig in a bias that limits the travel extent of the subreflector. Ideally, the subreflector actuators will be near their center of travel with the dish aligned at the rigging angle so that the full range of actuator motion is available to compensate for gravity and/or thermal errors. During the alignment process, only the dz and constant parameters are used in determining the best fit. Once the surface is aligned, the position of the subreflector is optimized using a best fit based on all of the parameters.

Surface errors are found by taking the difference between the best-fit paraboloid and the measured data. A typical contour plot of the surface HPLE and the associated histogram are shown in Figure 23. Red areas are protrusions from the desired surface, and blue areas are depressions into the desired surface. Figure 24 shows that the outer E ring has several subframes that appear
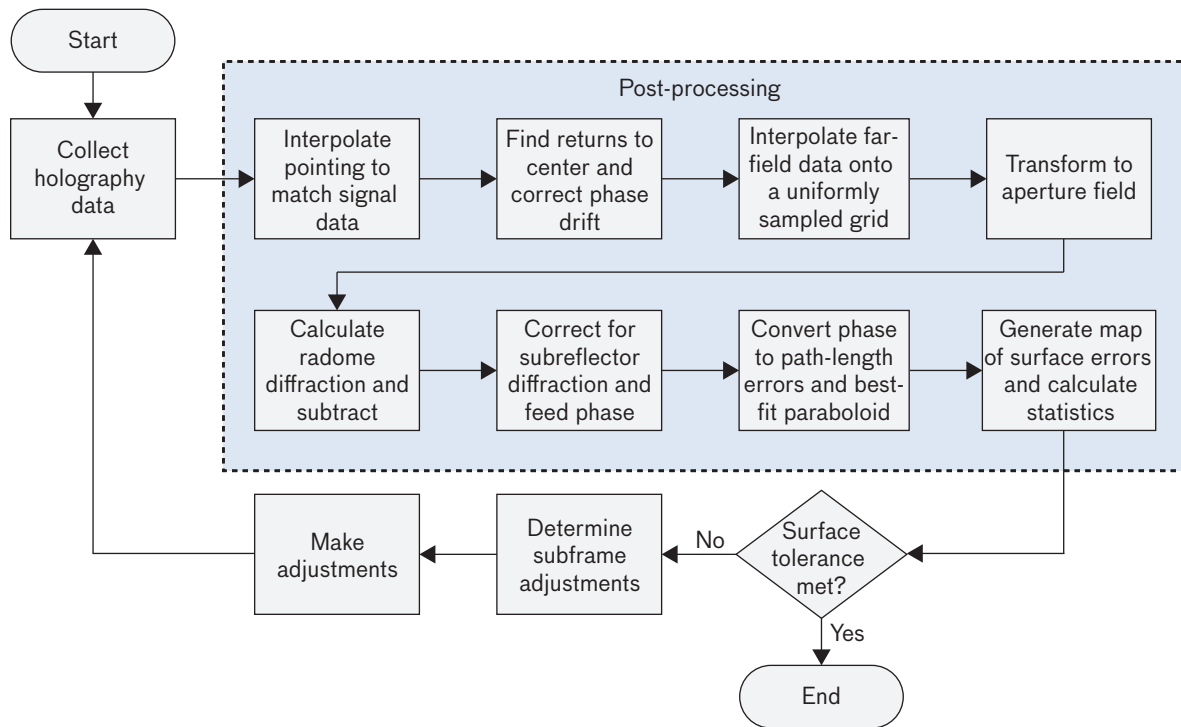
FIGURE 20. Correlation and antenna-pointing data are time-stamped and recorded. The data are post-processed using the steps shown above after the data collection is complete. Post-processing takes ~5 minutes using MATLAB on a laptop computer.

to be tilted and the middle C ring appears to be fairly well aligned. The histogram of the errors exhibits a bell-shaped curve that is similar to a normal distribution. The best-fit normal distribution shown in red highlights that the errors in this map are not entirely random.

Repeatability of the data is checked with multiple data collections each night. HPLE rms values were found to vary by 0 to 5 μm between data collections. This variation is due to measurement error and thermal variation. Measurement errors should be random across the aperture and those resulting from thermal variation should be correlated. To examine this correlation closer, plots of the differences between five consecutive data collections from the same night are shown in Figure 24. It only takes a few minutes to accurately determine the boresight direction to the satellite and to set up for the next scan, so the scans occur at 35-minute intervals.

Each single plot shows some regions are high and some regions are low. This variation suggests that the errors are correlated and are not predominantly random errors caused by low SNR. If the difference plots are compared to each other, a repeating pattern may be seen. The

first difference map (scan2-scan1) is higher at the top and lower at the bottom, the second difference map (scan3-scan2) is reversed with the top being lower and the bottom higher, the third (scan4-scan3) returns to the pattern of the first, and the fourth (scan5-scan4) resembles the second. This repeating behavior is believed to be due to thermal variations in the radome that correspond with cycling of the radome heating system.

The subframe adjustments were determined from the surface errors and the subframe adjustment basis functions shown in Figure 13. Measurements and adjustments were iterated until the limitations of the process were reached. A plot of the surface error as a function of iteration is shown in Figure 25. Thirteen iterations were completed and the limit of this alignment process appears to have been reached. The rms HPLE is seen to have converged to ~75 μm rms, corresponding to a one-way loss of antenna gain of 0.4 dB.

The final state of the surface is shown in Figure 26. The HPLE has been reduced to 75 μm rms and the errors are seen to be mostly random. The E ring has the largest errors. The E ring is the least stiff part of the structure,
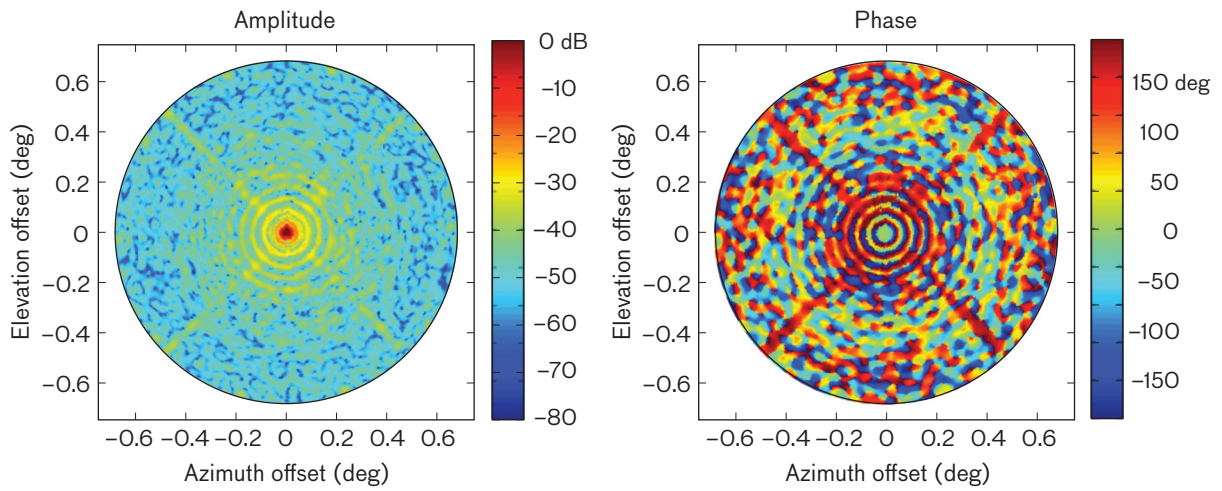
FIGURE 21. The normalized far-field pattern exhibits a central peak and rings of sidelobes. The effect of the quadrapod on the pattern is evident along the ±45 degree axes. The noise floor is on the order of 80 dB below the peak value.
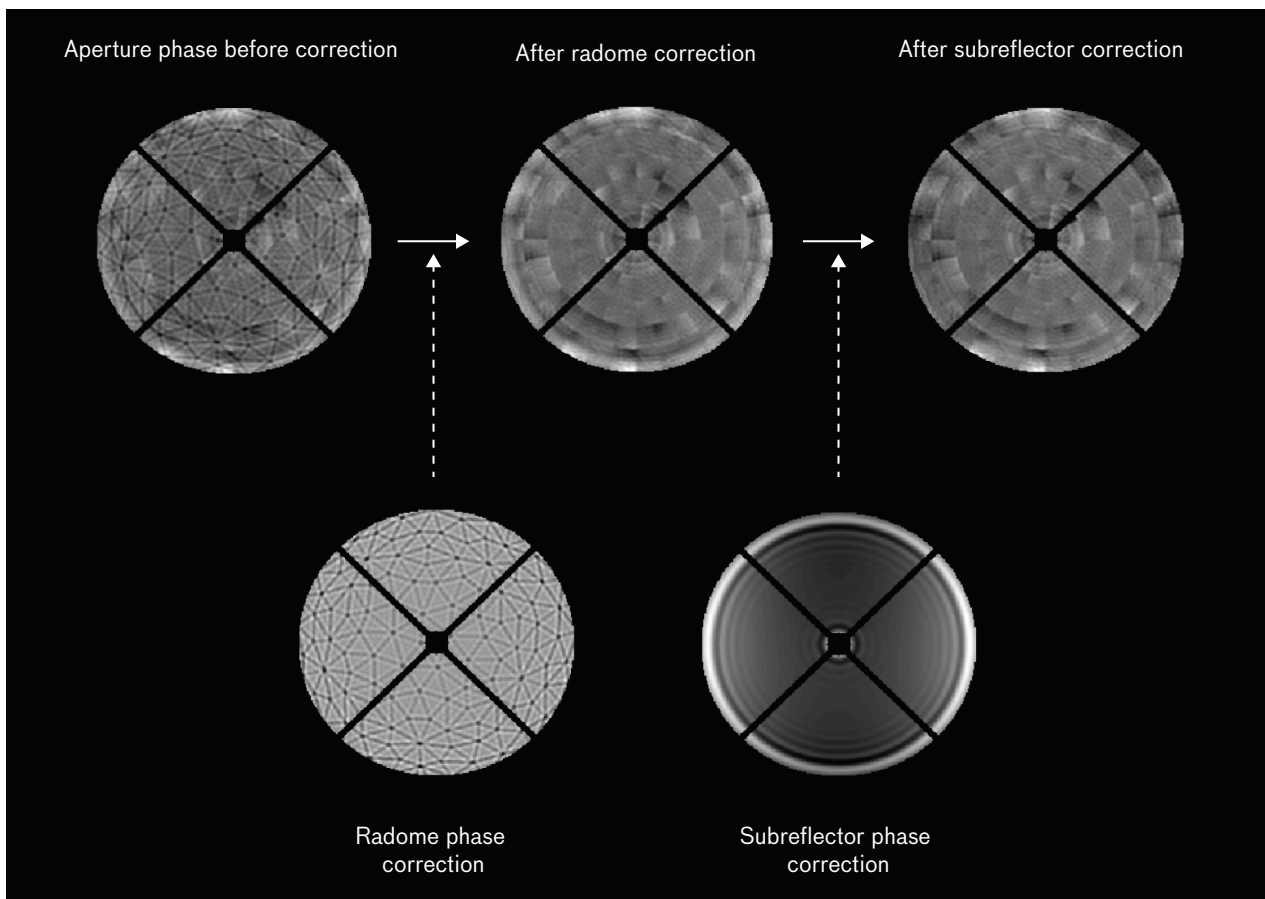

FIGURE 22. The phase of the aperture field is found by transforming the far-field pattern. The aperture field phase is then corrected to remove the effects of scattering from the radome spars and hubs and of diffraction from the subreflector. The region beneath the quadrapod legs is discarded and not used.
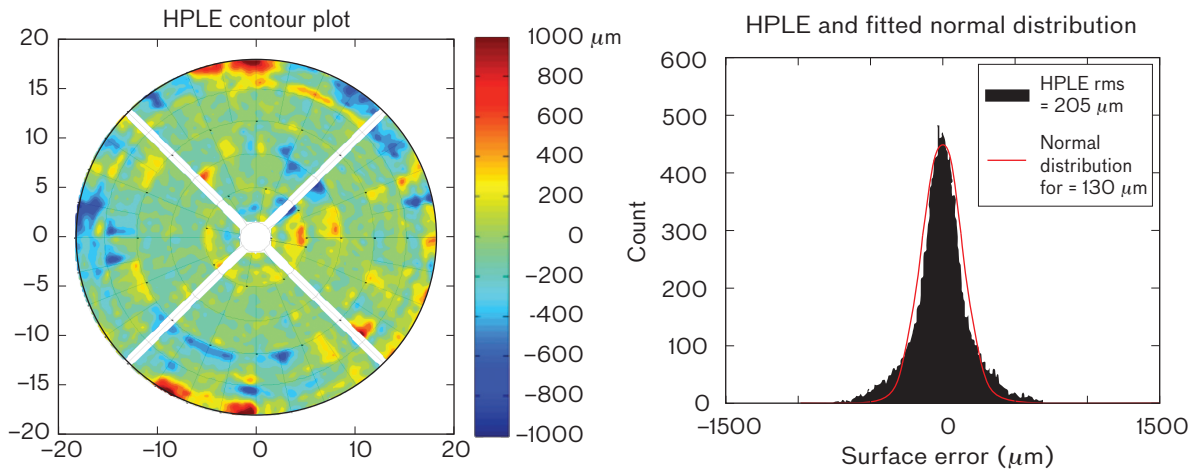
FIGURE 23. The difference between the best-fit paraboloid and the surface measurements may be visualized in a contour plot over the surface (axes are in meters). The red areas are high relative to the perfect paraboloid, and the blue areas are low. Ideally, the entire surface would be green. The distribution of errors may be seen in the histogram to the right.
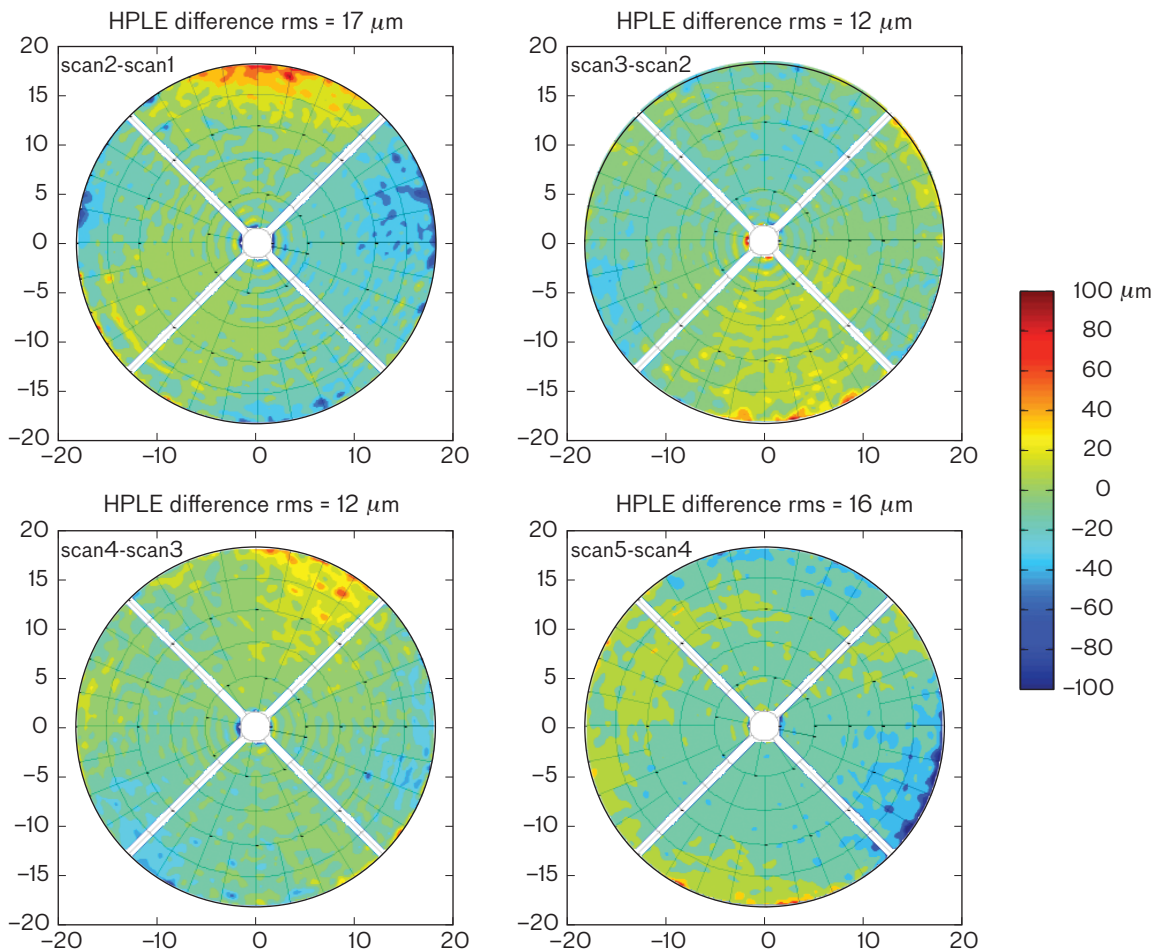

FIGURE 24. Data repeatability was checked by collecting several patterns sequentially and examining the differences between the HPLEs. The differences, found to be on the order of 15 μm rms, are consistent with a variation of 1 to 2 μm in the overall HPLE rms value between measurements. The errors are correlated and there appears to be a repeating pattern that coincides with cycling of the radome heating system.
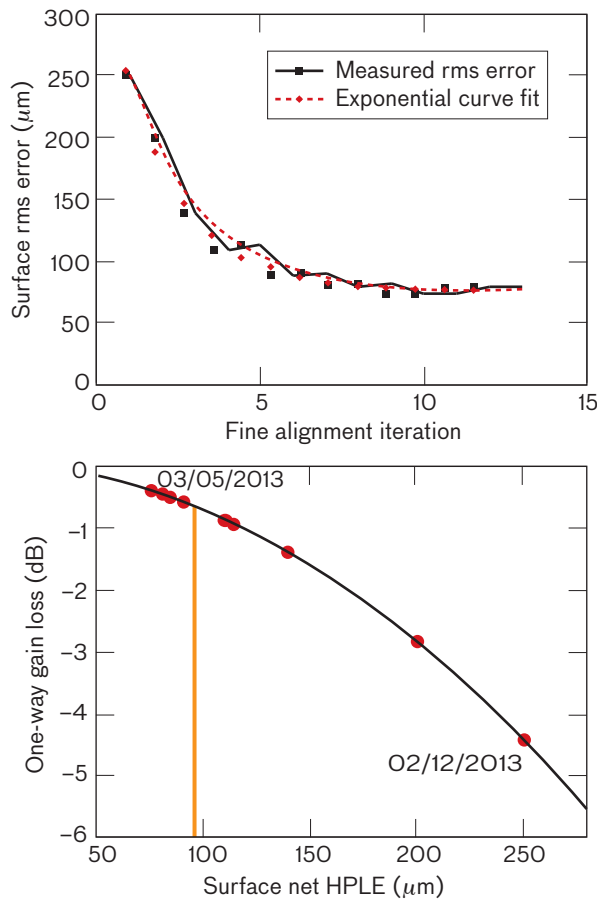
FIGURE 25. The process to align the surface was iterative. Holography measurements were conducted late at night, other radar integration tasks utilized the antenna during the day, and adjustments were made in the early evening. This process was repeated until the surface error converged. The final surface HPLE value achieved was 75 μm rms, which corresponds to 0.4 dB loss of gain compared to a perfect surface.

and it is also where the diffraction corrections from the subreflector are largest. Two concentric ridges appear to run along the E ring. These ridges were not seen in the subframe measurements collected when the panels were being aligned to the subframes. It is likely that these ridges are not real and are an artifact of the measurements and processing. The E ring is also where the illumination field is the lowest. The feed pattern is tapered such that the field is down ~10 dB at the edge of the dish compared to near the center, so the impact of errors in the E ring is lessened.

Conclusion

The 120-foot-diameter Haystack antenna was recently upgraded to accommodate the HUSIR W-band radar. To maximize efficiency, the surface of the new antenna is required to maintain a surface that deviates from a perfect paraboloid by 100 μm rms or less under all operating conditions. Having an efficient and precise method of measuring the surface is essential to achieve this objective. A microwave holography system was developed to meet this need. The HUSIR holography system is capable of generating a map of the surface errors that has a spatial resolution of 0.6 m and an accuracy of better than 20 μm in slightly less than half an hour. The holography system was utilized to iteratively align the surface of the HUSIR antenna, and a surface tolerance of 75 μm rms has been achieved.

The holography system is independent of the W-band radar. The system remains intact and is available to conduct measurements in support of surface maintenance. In addition to providing a map of the surface errors, the
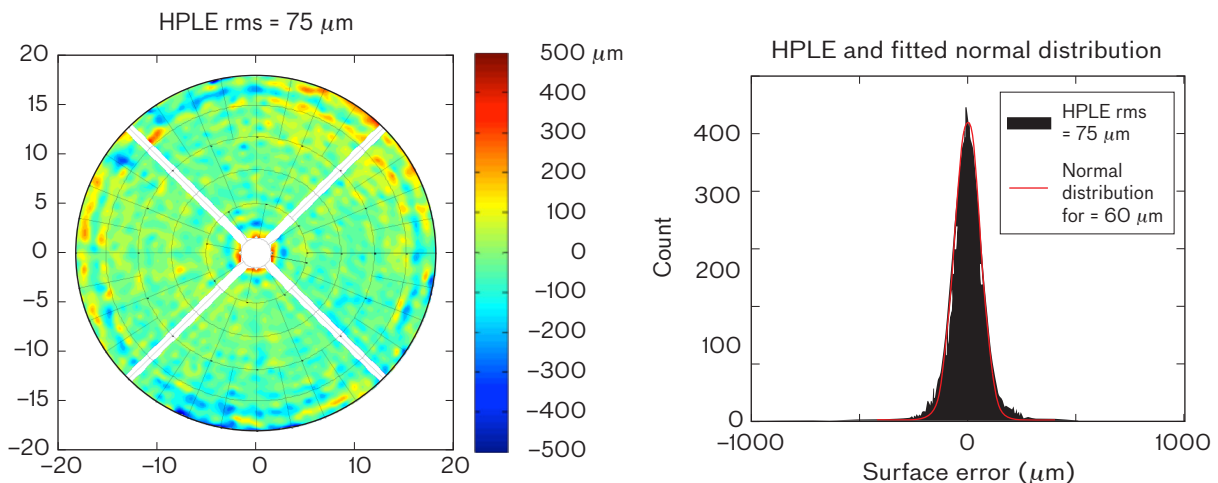

FIGURE 26. The surface alignment converged to this final state with an HPLE of 75 μm rms. The remaining errors are now mostly random. After alignment, the histogram of the errors more closely resembles a normal distribution.

best-fit paraboloid that is derived may be used to determine the optimal subreflector position. For operations at frequencies higher than W band, it would be beneficial to use holography to optimize the subreflector position before collecting data.

Acknowledgments

The authors wish to express our deepest gratitude to Alan Rogers for providing the radome and subreflector diffraction corrections and general advice and expertise on microwave holography, to Keith Doyle for developing the surface error budget and providing expertise on aligning optical systems, to John Peabody for developing the real-time processing hardware and software for the holography system, to Jay Eshbaugh for designing the holography RF receivers, and to Chris Kulig for helping with data collection and processing. ■

REFERENCES

1. J. Ruze, "Antenna Tolerance Theory—A Review," *Proceedings of the IEEE,* vol. 54, no. 4, 1966, pp. 633–640.
2. H.G. Weiss, "The Haystack Experimental Facility," MIT Lincoln Laboratory Technical Report 365, 1964.
3. H.G. Weiss, "The Haystack Microwave Research Facility," *IEEE Spectrum,* vol. 2, no. 2, 1965, pp. 50–69.
4. D.G. Stuart, "Haystack Antenna Reflector Surface Improvement Program," MIT Lincoln Laboratory Technical Note 1968-7, 29 January 1968.
5. R.P. Ingalls et al., "Upgrading the Haystack Radio Telescope for Operation at 115 GHz," *Proceedings of the IEEE,* vol. 82, no. 5, 1994, pp. 742–755.
6. M.S. Zarghamee, J. Antebi, and F.W. Kan, "Optimal Surface Adjustment of Haystack Antenna," *IEEE Transactions on Antennas and Propagation,* vol. 43, no. 1, 1995, pp. 79–86.
7. K.B. Doyle et al., "RF-Mechanical Performance for the Haystack Radio Telescope," *Proceedings of SPIE*, vol. 8125, 2011, pp. 81250A-1–81250A-9.
8. S. von Hoerner, "Design of Large Steerable Antennas," *The Astronomical Journal,* vol. 72, no. 1, 1967, pp. 35–47.
9. J. Antebi and F.W. Kan, "Replacement of Elevation Structure to Upgrade Haystack 37-m Radio Telescope," *Proceedings of SPIE,* vol. 5495, 2004, pp. 137–146.
10. M.E. MacDonald, "Measured Thermal Dynamics of the Haystack Radome and HUSIR Antenna," *IEEE Transactions on Antennas and Propagation,* vol. 61, no. 5, 2013, pp. 2441–2448.
11. K.B. Doyle, "Antenna Performance Predictions of a Radio Telescope Subject to Thermal Perturbations," *Proceedings of SPIE,* vol. 7427, 2009, pp. 74270D-1–74270D-9.
12. J.C. Bennett, A.P. Anderson, P.A. McInnes, and A.J.T. Whitaker, "Investigation of the Characteristics of a Large Antenna Using Microwave Holography," *Proceedings of IEEE Antennas and Propagation Society International Symposium,* vol. 11, 1973, pp. 298–301.
13. J.C. Bennett, A.P. Anderson, P.A. McInnes, and A.J.T. Whitaker, "Microwave Holographic Metrology of Large Reflector Antennas," *IEEE Transactions on Antennas and Propagation,* vol. 24, no. 3, 1976, pp. 295–303.
14. P.F. Scott and M. Ryle, "A Rapid Method for Measuring the Figure of a Radio Telescope Reflector," *Monthly Notices of the Royal Astronomical Society,* vol. 178, 1977, pp. 539–545.
15. C.E. Mayer et al., "A Holographic Surface Measurement of the Texas 4.9-m Antenna at 86 GHz," *IEEE Transactions on Instrumentation and Measurement,* vol. 32, no. 1, 1983, pp. 102–109.
16. Y. Rahmat-Samii, "Surface Diagnosis of Large Reflector Antennas Using Microwave Holographic Metrology: An Iterative Approach," *Radio Science,* vol. 19, no. 5, 1984, pp. 1205–1217.
17. D. Morris, J.W.M. Baars, H. Hein, H. Steppe, C. Thum, and R. Wohlleben, "Radio-Holographic Reflector Measurement of the 30-m Millimeter Radio Telescope at 22 GHz with a Cosmic Signal Source," *Astronomy and Astrophysics,* vol. 203, no. 2, 1988, pp. 399–406.
18. D.J. Rochblatt and B.L. Seidel, "DSN Microwave Antenna Holography," TDA Progress Report 42-76, Pasadena, Calif.: JPL, 1983, pp. 27–42.
19. D.J. Rochblatt and B.L. Seidel, "Microwave Antenna Holography," *IEEE Transactions on Microwave Theory and Techniques,* vol. 40, no. 6, 1992, pp. 1294–1300.
20. D.J. Rochblatt, "Chapter 8: Microwave Antenna Holography," in *Low-Noise Systems in the Deep Space Network,* M.S. Reid, ed. Hoboken, N.J.: Wiley, 2008.
21. S. Silver, *Microwave Antenna Theory and Design.* New York: McGraw-Hill, 1949.
22. A. Rogers, R. Barvainis, P. Charpentier, and B. Corey, "Corrections for the Effects of a Radome on Antenna Surface Measurements Made by Microwave Holography," *IEEE Transactions on Antennas and Propagation,* vol. 41, no. 1, 1993, pp. 77–84.

ABOUT THE AUTHORS

Joseph M. Usoff is a senior staff member in Lincoln Laboratory's Aerospace Sensor Technology Group. Since joining Lincoln Laboratory in 1993, he has performed missile seeker testing, developed an automated radar cross section diagnostic tool for stealth aircraft, developed and implemented real-time radar imaging algorithms, and, most recently, contributed to the Haystack Ultrawideband Satellite Imaging Radar project. Prior to his Laboratory career, he worked at Raytheon as an antenna engineer, at the U.S. Air Force Radar Target Scatter Facility (RATSCAT) as the chief data analyst, and at The Ohio State University ElectroScience Laboratory as a graduate researcher. He earned a bachelor's degree in electrical engineering from Carnegie Mellon University and master's and doctoral degrees in electrical engineering from The Ohio State University.

Michael T. Clarke is an associate technical staff member in the Aerospace Sensor Technology Group. Since joining the Laboratory in 2006, he has worked on several radar systems at sites including the National Radio Astronomy Observatory in Greenbank, West Virginia; the Reagan Test Site in Kwajalein, Marshall Islands; and most predominantly, the Lincoln Space Surveillance Complex in Westford, Massachusetts. He received bachelor's and master's degrees, both in electrical engineering, from the University of Massachusetts.

Chao Liu was an assistant technical staff member in the Aerospace Sensor Technology Group. She joined the Laboratory after graduating from the California Institute of Technology with a bachelor's degree in physics. During her two years in the group, her main research focus was the development of HUSIR microwave antenna holography. She has also worked on the through-the-wall radar and multistatic radar projects. Since returning to school in 2012 at Stanford University, she has completed a master's degree in medicine and is currently pursuing a doctoral degree in biochemistry. Her research uses biophysical techniques to study hypertrophic cardiomyopathy, a common inherited heart disease.

Mark J. Silver is a member of the technical staff in the Mechanical Engineering Group. Since joining Lincoln Laboratory in 2010, his work has included structural design, analysis, and testing for the Lunar Laser Communication Demonstration, the HUSIR antenna, and the high-energy laser programs. Prior to joining Lincoln Laboratory, he worked on deployable spacecraft structures research at QinetiQ North America in Waltham, Massachusetts. He received a bachelor's degree in engineering mechanics from the University of Wisconsin in 1999, and master's and doctoral degrees in aerospace engineering from the University of Colorado in 2001 and 2005, respectively; his graduate research focused on deployable spacecraft structures and the mechanics of thin composite materials.